ARTICLE IN PRESS

Nature Communications

https://doi.org/10.1038/s41467-026-70727-2

Article in Press

Programmable ferroelectric rectifier for reliable and efficient neuromorphic crossbar array

Received: 29 August 2025

Accepted: 28 February 2026

Cite this article as: Kim, Y., Lee, Y.J., Yang, J. *et al.* Programmable ferroelectric rectifier for reliable and efficient neuromorphic crossbar array. *Nat Commun* (2026). https://doi.org/10.1038/s41467-026-70727-2

Youngmin Kim, Yoon Jung Lee, Jiwoong Yang, Byungsoo Kim, Seung Ju Kim, Jaehyun Kim, Inhyuk Im, Jae Young Kim, He Rui, Haesung Kim, Chung Wung Bark, Min Hyuk Park, Dae Hwan Kim, Sung-Jin Choi, J. Joshua Yang, Sanghan Lee & Ho Won Jang

We are providing an unedited version of this manuscript to give early access to its findings. Before final publication, the manuscript will undergo further editing. Please note there may be errors present which affect the content, and all legal disclaimers apply.

If this paper is publishing under a Transparent Peer Review model then Peer Review reports will publish with the final article.

ARTICLE IN PRESS

© The Author(s) 2026. **Open Access** This article is licensed under a Creative Commons Attribution-NonCommercial-NoDerivatives 4.0 International License, which permits any non-commercial use, sharing, distribution and reproduction in any medium or format, as long as you give appropriate credit to the original author(s) and the source, provide a link to the Creative Commons licence, and indicate if you modified the licensed material. You do not have permission under this licence to share adapted material derived from this article or parts of it. The images or other third party material in this article are included in the article's Creative Commons licence, unless indicated otherwise in a credit line to the material. If material is not included in the article's Creative Commons licence and your intended use is not permitted by statutory regulation or exceeds the permitted use, you will need to obtain permission directly from the copyright holder. To view a copy of this licence, visit http://creativecommons.org/licenses/by-nc-nd/4.0/.

Article type: Research Article

Programmable ferroelectric rectifier for reliable and efficient neuromorphic crossbar array

*Youngmin Kim‡[1], Yoon Jung Lee‡[1,2,3], Jiwoong Yang‡[4], Byungsoo Kim[1], Seung Ju Kim[5], Jaehyun Kim[1], Inhyuk Im[1], Jae Young Kim[1], He Rui[6], Haesung Kim[3], Chung Wung Bark[6], Min Hyuk Park[1], Dae Hwan Kim[3], Sung-Jin Choi[3], J. Joshua Yang[*5], Sanghan Lee[*4], and Ho Won Jang[*1,7]*

‡ These authors contributed equally to this work

[1]Department of Materials Science and Engineering,
Research Institute of Advanced Materials,
Seoul National University,
Seoul 08826, Republic of Korea

[2]Department of Chemistry
Northwestern University,
Evanston IL 60208, United States

[3]School of Electrical Engineering,
Kookmin University,
Seoul 02707, Republic of Korea

[4]Department of Materials Science and Engineering,
Gwangju Institute of Science and Technology,
Gwangju 61005, Republic of Korea

[5]Ming Hsieh Department of Electrical and Computer Engineering,
University of Southern California,
Los Angeles California 90089, United States

[6]Department of Electrical Engineering,
Gachon University,
Seongnam-si, Gyeonggi-do 13120, Republic of Korea

[7]Advanced Institute of Convergence Technology,
Seoul National University,
Suwon 16229, Republic of Korea

[*]Corresponding authors. E-mail: jjoshuay@usc.edu, sanghan@gist.ac.kr, hwjang@snu.ac.kr

ARTICLE IN PRESS

ARTICLE IN PRESS

Abstract

The advancement of neuromorphic computing hardware requires energy-efficient operation, scalable device integration, and reliable conduction. These challenges can be effectively addressed by employing functional ferroelectric material as an active layer in memristors, leveraging their electrostatically modulated conduction for reliable switching. In this study, we present memristor devices that achieve a rectifying ratio exceeding 10^6 and an off-state current below 10^{-12} A based on epitaxial heterostructures consisting of Pt/$Ba_{0.2}Bi_{0.8}FeO_3$ (BBFO)/$SrRuO_3$/$SrTiO_3$ stacks. Substitution of 20% Ba in $BiFeO_3$ induces a coupled interaction between ferroelectric polarization and oxygen vacancy migration, which under pulsed bias governs vacancy transport and ensures reliable memristive synaptic behavior with near-zero nonlinearity and endurance beyond 10^7 cycles. Owing to the demonstrated linear synaptic performance and strong memristive rectification, a selector-free crossbar array (CBA) was implemented. By mitigating key CBA challenges such as sneak currents and cell-to-cell variability while maintaining high synaptic performance, BBFO provides a robust material platform for CBA-based neuromorphic systems.

ARTICLE IN PRESS

ARTICLE IN PRESS

Introduction

In the post-Von Neumann era, the development of neuromorphic computing hardware based on artificial neural networks (ANNs) has become a critical focus in advancing next-generation semiconductor technologies. While complementary metal oxide semiconductors (CMOS)-based platforms have played a pivotal role in accelerating artificial intelligence (AI) technologies [1-4], there is an increasing need to overcome their inherent limitations. These limitations primarily arise from high energy consumption and challenges in device scaling. To overcome these bottlenecks, developing more energy-efficient and scaling-compatible alternatives is essential.

Among the candidates to overcome these challenges, memristors are promising structures that show low operation voltages and fast programming/erase speed. [5] Additionally, multilevel conductance tunability for storing multi-bit data has been demonstrated [6, 7], along with high integration density at the sub-2 nm scale, which is compatible with recent CMOS technologies [8-10] . Leveraging these properties, artificial synaptic elements in neuromorphic systems have been widely developed using various memristor types by alternating insulator layers such as halide perovskites [11-13], phase change materials [14, 15], or electrochemical oxide materials. [9] These materials have been characterized by their own ionic motions in the nonvolatile manner, showing multi-level resistive change in collaborative conduction mediums within regularly aligned lattice structures. [16-19]

However, this conduction mechanism is often hindered by reliability issues, such as random distribution of ions/vacancies [20], inconsistent device-to-device performance [21], and nonlinear programming behaviors [22] even considering an application of highly crystalline active layer. Furthermore, the ambipolar switching behavior observed in typical memristors renders crossbar

ARTICLE IN PRESS

ARTICLE IN PRESS

array (CBA) fabrication—an ideal memory architecture in in-memory computing (IMC) systems [19]—vulnerable to sneak currents. This leakage undermines cell selectivity [20], leading to degraded CBA programming functionality and increased processing costs [21] due to the need to integrate a selector device with each memory cell. These challenges in recent memristors technologies impede the further advancement of CBA integration. Therefore, it is imperative to explore self-rectifying memristor designs with reliable conduction mechanisms for the practical application of CBAs in neuromorphic computational systems. [23-31]

In this article, we demonstrate the implementation of highly rectifying electrical performance with an on/off ratio surpassing 10^6 using a two-terminal memristor structure composed of Pt/$Ba_{0.2}Bi_{0.8}FeO_3$ (BBFO)/$SrRuO_3$ (SRO)/$SrTiO_3$ (STO) epitaxial heterostructures. By incorporating 20 % Ba into the ferroelectric material $BiFeO_3$ (BFO), we reveal a dynamic interplay between ferroelectricity and oxygen vacancy migration, enabling rectifying *J–V* performance and linear synaptic performance.

ARTICLE IN PRESS

In the rectifying *J–V* performance, additional dipole stemming from the oxygen vacancy migration contributes to Schottky- and Ohmic-like conduction at the BBFO/SRO and BBFO/Pt interfaces, respectively. Of course, such alternation is not limited to rectifying memristors; however, in our case, the rectification primarily originates from the coupling between ferroelectric polarization and oxygen vacancy modulation. The homogeneous variation in the migration velocity of oxygen vacancies, governed by the ferroelectric electrostatic field, leads to an enhanced on/off current ratio in the *J-V* characteristics. Negative dipoles are induced in conjunction with the annihilation of oxygen vacancies by oxygen ion compensation from the SRO side, while positive dipoles arise along with the accumulation of oxygen vacancies near the Pt interface. Variations in

ARTICLE IN PRESS

oxygen vacancy density in BBFO modify the ferroelectric polarization. The resulting change enables effective modulation of the interface barrier profiles, supporting consistent device behavior and high performance. Beyond its self-rectifying capability, the device shows reliable artificial synaptic behavior, characterized by regular charge migration with near-zero nonlinearity. Furthermore, linearly programmable synaptic responses are achieved through ferroelectric modulation, which retards vacancy migration and prevents fast saturation depending on the voltage pulses. Benefiting from artificial synapses capable of enduring over 10^7 repeated weight updates, we successfully implement a selector-free CBA consisting of 11×11 BBFO memristor cells. Our strategy enables the theoretical integration of up to 2.6×10^9 cells within a densely integrated crossbar array architecture, maintaining a 10% readout margin. These findings suggest that epitaxially grown BBFO films are promising memristive materials for ultra-dense neuromorphic computing architectures, enabling robust crossbar integration and reliable synaptic functionality within in-memory systems.

ARTICLE IN PRESS

Results

Crossbar array device based on epitaxial ferroelectric materials

Figure 1 shows a comprehensive summary of the characteristics of the CBA based on an epitaxially grown BBFO ferroelectric film. As illustrated in Figure 1a, the CBA consists of a stacked structure of Pt word lines/BBFO/SRO bit lines on a (001) STO substrate. In this configuration, BBFO serves as the active layer of the memristor, while SRO acts as the bottom electrode. According to Supplementary figure 1, the cross-sectional energy dispersive spectroscopy (EDS) image, obtained during transmission electron microscopy (TEM) observation, clearly distinguishes the individual layer, revealing thicknesses of 100 nm and 40 nm for BBFO

ARTICLE IN PRESS

and SRO, respectively. The CBA comprises 121 memory cells, arranged in an 11 × 11 crossbar matrix, patterned within a 1cm × 1cm STO substrate (Figure 1b). Notably, our CBA demonstrates unidirectional current flow from the top electrode to bottom electrode, enabling selective reading target memristor cells while effectively blocking parasitic current. This asymmetric current flow is consistently observed in every memristor cells, ensuring excellent cell-to-cell uniformity. This device reproducibility can be attributed to sophisticatedly controlled defects across a substrate due to the epitaxial heterostructures.

High-angle annular dark field scanning transmission electron microscopy (STEM-HAADF) imaging was performed to confirm the epitaxial growth of the configured layers (Figure 1c). This image reveals periodically aligned atomic arrangements in BBFO and SRO, with atomic distances of 0.596 nm and 0.618 nm at the A-site (Sr and Ba/Bi atoms) and B-site (Fe, Ru, and Ti atoms) in oxide perovskite structure (ABO_3), respectively. Additionally, Supplementary figures 2a and 2b reveal clear atomic differentiation between BBFO and SRO, together with pronounced Ba substitution confirmed by EDS mapping, indicating that the BBFO film grows uniformly from the interface. Furthermore, Supplementary figure 2c presents a globally measured STEM-HAADF image of the BBFO film, which confirms that the pristine polarization direction is downward. The fast Fourier transform (FFT) images in Supplementary figure 2d further verify the distinct crystallographic character. The electron backscattered diffraction (EBSD) image of Pt/BBFO/SRO device (as shown in Supplementary figure 3) further supports the uniformity of epitaxial BBFO film. Beyond TEM analyses, X-ray diffraction (XRD) measurements were conducted including theta-2theta, phi-scans, and reciprocal space mapping (RSM) (Supplementary figures 4a-4c). Based on these results, we conclude that the BFO and BBFO were grown epitaxially while simultaneously undergoing compressive strain along the in-plane direction. The BBFO possesses

ARTICLE IN PRESS

greater compressive strain, which is attributed to the larger atomic radius of the substituting Ba compared to Bi. (Supplementary figure 4d) The c-axis expanded structure maintains stability even under high concentrations of barium substitution, and this strained structure effectively suppresses oxygen diffusion, enabling stable resistive modulation. [32-34]

The rectification properties of an individual memristor unit are evident in its memristive *J*-*V* curve, which exhibits clockwise current modulation and a high rectifying ratio exceeding 10^5 between the low resistance state (LRS) and high resistance state (HRS) (Figure 1d). Thanks to the significantly suppressed leakage currents in BBFO induced by charge canceling provided from SRO oxygen ions, an ultra-low current level ($< 10^{-12}$ A) in the HRS region is achieved, contributing to the high rectification ratio. Additionally, the interplay between ferroelectricity and oxygen vacancies dynamically modulates the energy barrier at BBFO/SRO and Pt/BBFO junctions. Notably, the velocity of oxygen vacancy migration can be controlled by ferroelectric polarization. Gradually facilitating oxygen vacancy migration, ferroelectricity induces velocity change of oxygen vacancies. This dynamically changed charge migration induces linearly modulated synaptic performance, as illustrated in Figure 1e. In contrast to the typical LTP/LTD curve, represented by the red dotted line in Figure 1e, our linearly modulated curves originate from the coupling effect between oxygen vacancies and ferroelectricity. A detailed explanation will be provided in Figure 3d. As a result of this phenomenon, we obtain highly linear long-term potentiation/depression (LTP/LTD) performances across 39 memristor devices (Figure 1f). Using these reliable memristor devices, CBA fabrication is implemented. As shown in Figure 1g, a clear letter B pattern was obtained by applying a multiply–accumulated (MAC) operation at the S_3 column in the cell matrix. This obvious text image is primarily attributed to the uniform conductance modulation across all memristor cells, ensuring consistent conductance gap achieved

ARTICLE IN PRESS

by voltage pulses ranging from 10 to 100 (Figure 1h).

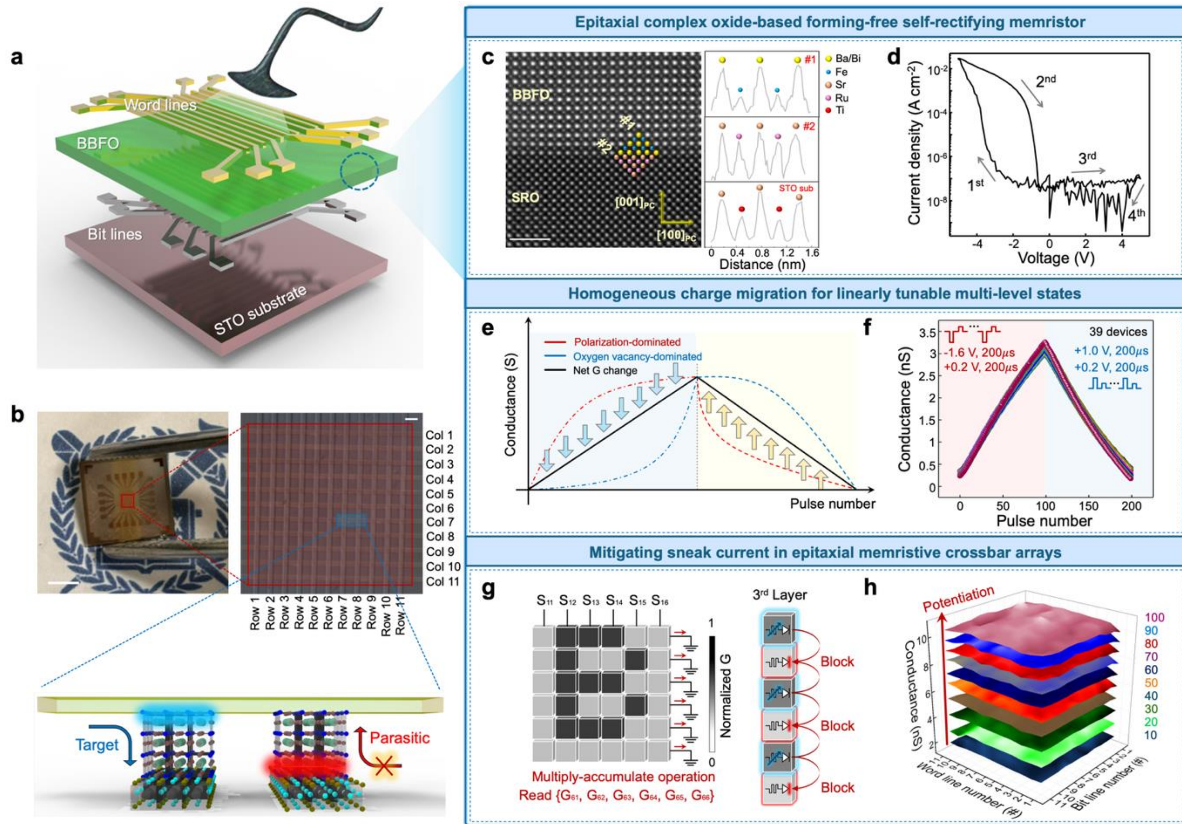

Figure 1. Comprehensive summary of this study a) Schematic illustration of the CBA structure. **b)** OM image of the CBA sample and SEM image of CBA memristor cells. The scale bars for the device image and OM image are 4 mm and 100 µm, respectively. Two parallel memristor cells are shown, highlighting the target and parasitic current paths. The parasitic current path is blocked by the rectifying current in BBFO. **c)** STEM-HAADF image of the BBFO/SRO interface. The scale bars is 2nm. **d)** Memristive *J-V* characteristics measured under a bias range of −5 V to +5 V with the SRO electrode grounded. **e)** Schematic representation of the LTP and LTD behaviors governed by ferroelectric polarization and oxygen vacancies in BBFO. **f)** Cell-to-cell variation in LTP and LTD characteristics evaluated using dot-patterned electrode-devices configured with 39 individual cells. The applied voltage pulses for LTP and LTD measurement were -1.6 V/+1.0 V, with a read voltage of 0.2 V and a pulse duration of 200 µs, **g)** Conductance mapping image displaying the letter B in the selector-free CBA, with the blocked sneak path at S_{13} column illustrated alongside the text image. h) Conductance mapping of individual memristor cells in the 11 x 11 CBA, ranging from 1.98 nS to 10.8 nS, as the number of applied voltage pulses varied from 10 to 100 in increments of 10.

Self-rectifying electrical performances

The rectification mechanism of BBFO was investigated by analyzing its electrical performance. Using a unit memristor composed of Pt/BBFO/SRO shown in Figure 2a, we conducted multiple

ARTICLE IN PRESS

J-V measurements. Interestingly, the *J-V* characteristics (Figure 2b) exhibited robust endurance, maintaining a high rectifying ratio exceeding 10^5 for over 100 consecutive cycles. This high rectification cannot be achieved if the applied voltage sweep is either below or beyond ±5 V (Supplementary figure 5). For voltage ranges lower than ±5V (Supplementary figure 5a), the LRS current level is significantly reduced compared to that of Figure 2b. Furthermore, for voltage ranges exceeding ±5 V, the HRS current is more increased than that of Figure 2b, leading to a decrease in rectifying ratio (Supplementary figure 5b). These findings highlight that a precise voltage range of ±5 V is critical to achieving optimal self-rectification in BBFO memristors. Supplementary figure 6 shows that the BBFO device can exhibit filamentary-type behavior, but only after electroforming under a high positive bias of +28 V. In contrast, the BBFO memristor investigated in the present study operates in a forming-free manner within a voltage window below ±5 V. The comparison indicates that oxygen vacancies can participate in the BBFO device operation mechanism, yet their contribution is manifested as interface-modulated resistive switching rather than localized filament formation.

ARTICLE IN PRESS

The endurance of ferroelectricity in BBFO was assessed through polarization endurance measurements, applying a voltage sequence from 0 V to 5 V, returning to 0 V, stepping to −5 V, and returning to 0 V (Supplementary Figure 7a). Even after 10^8 cycles, the remnant polarization (P_r) exhibited minimal degradation, demonstrating excellent ferroelectricity stability. The P_r during the polarization endurance test was changed from 55.7 μCcm^{-2}, 47.7 μCcm^{-2} (Supplementary figures 7b-7c) to 41.8 μCcm^{-2} (Figure 2c) after measuring the most initial stage, 10^4 cycles, and 10^8 cycles, respectively. The STEM-HAADF image in the inset of Figure 2c further confirms the robust downward polarization of BBFO. We performed out-of-plane piezoelectric force microscopy (PFM) under an applied voltage of ± 10 V to investigate the polarization

ARTICLE IN PRESS

characteristics (Supplementary figures 8a-8d). A clear double-window pattern was observed in both phase and amplitude PFM images, confirming the strong piezoresponse by ±10 V. The opposite phase under reverse voltage polarity was distinctly differentiated, while protrusion in the phase signal was evident at the outer window region under +10 V application (Supplementary figure 8e).

Additionally, we conducted X-ray photoelectron spectroscopy (XPS) analysis to quantify the oxygen vacancy (V_O) concentration in BBFO (Supplementary figures 9a-9c). The results revealed that oxygen vacancies in BBFO originate from Ba–O bonding. The XPS peak observed at 531 eV, ascribed to Ba–O–Ba bonding, is related to the Ba 3*d* signal observed at 779.5 eV. [35] The Ba-O-V_O bond, characterized by a binding energy of 778.5 eV, indicates that oxygen vacancies can be generated by Ba substitution within the lattice. These results suggest that barium alloying may serve as an effective method for generating oxygen vacancies, providing a more controllable approach to vacancy incorporation than that arising from unstable Bi bonding. Based on our XPS results, the oxygen vacancy ratios in BFO and BBFO were calculated to be 6% and 8%, respectively (Supplementary figure 9b). These results suggest that Ba incorporation increases the concentration of mobile oxygen vacancies, potentially contributing to the resistive switching mechanism in the BBFO film. Based on the depth profile of the BBFO/SRO/STO heterostructures (Supplementary figure 9d), it can be further confirmed that Ba and Bi are uniformly alloyed in BBFO at a ratio of 1:4.

A band diagram illustrating electron flow under different applied voltages was constructed to investigate the electrical rectification mechanism. The bandgap and band alignment information used for band diagram illustration were obtained from ultraviolet photoelectron spectroscopy (UPS)

ARTICLE IN PRESS

ARTICLE IN PRESS

and UV-visible spectroscopy (Supplementary figures 10a, 10b). The switching process follows 4 sequential steps, corresponding to the 4 processes denoted in Figure 2d. [5] 1) At the initial stage, a negative voltage (on Pt electrode) drives oxygen vacancies toward the Pt/BBFO interface, inducing the upward band bending. **2)** When the negative voltage reaches close to -5 V, oxygen vacancies are migrated toward the BBFO/Pt interface, leading to sharp upward band bending. The accumulation of oxygen vacancies within BBFO may enhance the effectiveness of positive dipoles by coupling with the intrinsic dipoles. Such dipolar interactions could reinforce the ferroelectric response, potentially leading to an increased upward polarization magnitude. This correlation where the migrated oxygen vacancies increase magnitude of upward polarization mainly contributes to the Ohmic-like conduction at BBFO/Pt interface, despite the sharp upward energy barrier at Pt/BBFO. Supplementary figures 11a-11c also enforces the Ohmic conduction behavior at Pt/BBFO induced by the accumulation of oxygen vacancies, by showing opposite rectifying behavior when applying ground to the SRO electrode. The minimized hysteresis observed in Supplementary figure 11c, where SRO electrodes capable of supplying oxygen ions are used for both the top and bottom contacts, indirectly suggests that oxygen vacancy migration contributes to the device mechanism. Furthermore, the Schottky emission fitting in Supplementary figure 12 reveals that the effective barrier height differs between the LRS and HRS, indicating that resistance switching involves changes in oxygen vacancy distribution or polarization state. A significant barrier reduction occurs during the transition from HRS to LRS under negative voltage sweep. 3) Upon applying a positive voltage, oxygen vacancies begin to deplete at the BBFO/Pt interface. At this step, additional oxygen ions from the SRO electrode neutralize the charges of migrating oxygen vacancies, resulting in a depletion region near the BBFO/SRO interface. Even with sufficient electron supply from SRO, the interface barrier height of 0.77 eV between BBFO and

ARTICLE IN PRESS

ARTICLE IN PRESS

SRO is large enough to block electron transport unless oxygen vacancies are present to significantly narrow the barrier width. **4)** As the positive voltage increases to +5 V, the polarization switches downward, and the resulting vacancy-depleted region helps maintain stable rectification by suppressing leakage pathways. The enhanced oxygen ion flow further expands this depletion region within the BBFO layer, leading to a flatter band structure compared to earlier steps. The resulting charge deficiency within BBFO may also contribute to internal negative dipole formation. Consequently, the increased downward polarization facilitates Schottky conduction during *J*–*V* sweeping. XPS analysis in Supplementary figure 13 was conducted after removing the top electrodes of devices in both LRS and HRS states. In the LRS state, oxygen vacancy accumulation toward the top side (attributed to barium doping) was observed. Supplementary figure 14 presents the extracted activation energy required for device operation, showing an Arrhenius fitting result of approximately 0.4 eV. Supplementary figure 15 compares the effective oxygen-vacancy diffusion coefficients by extracting the activation energy in the same manner for the undoped BFO device. The results are $5 \times 10^{-21}\ \mathrm{m^2\ s^{-1}}$ for BFO and $9 \times 10^{-22}\ \mathrm{m^2\ s^{-1}}$ for BBFO at room temperature, indicating the robustness of BBFO, which does not permit higher leakage currents than BFO over the investigated temperature range. [32]

Supplementary figure 16 where the negative voltage of -5 V for the upward poling leads to higher on/off current ratio gives further persuasion that the asymmetrically high current magnitude in the negative voltage range. Supplementary Note 1 explains much detailed self-rectifying electrical behaviors induced by ferroelectricity-oxygen vacancy interaction.

Notably, the high rectification can be proven even under various voltage sweep velocity, voltage range, and ambient temperature (Supplementary figure 17). Additionally, the maintained

ARTICLE IN PRESS

ARTICLE IN PRESS

rectification ratio and direction, even when using different TE materials including Ag, Ti, and Au further supports that the observed asymmetric electrical conduction cannot be explained by metal ion diffusion or Schottky diode effect, but rather to the intrinsic conduction mechanism of the BBFO material (Supplementary figure 18). Furthermore, deep-level transient spectroscopy (DLTS) measurements (Figure 2e, Supplementary figures 19a-19b, Supplementary Note 2) revealed trap density (n_T) can be shown as 4.75×10^{17} cm^{-3} when assuming effective density of states in conduction band (N_c) as 10^{19} cm^{-3}. [36] Based on the DLTS parameters summarized in Supplementary Table 1, the results also revealed the presence of a shallow trap state located approximately 0.074 eV below the conduction band edge. This energy level is consistent with donor-like traps and is likely associated with oxygen vacancies acting as shallow donors in the BBFO matrix. Figure 2f presents a schematic energy band diagram reflecting the presence of these shallow trap states.

ARTICLE IN PRESS

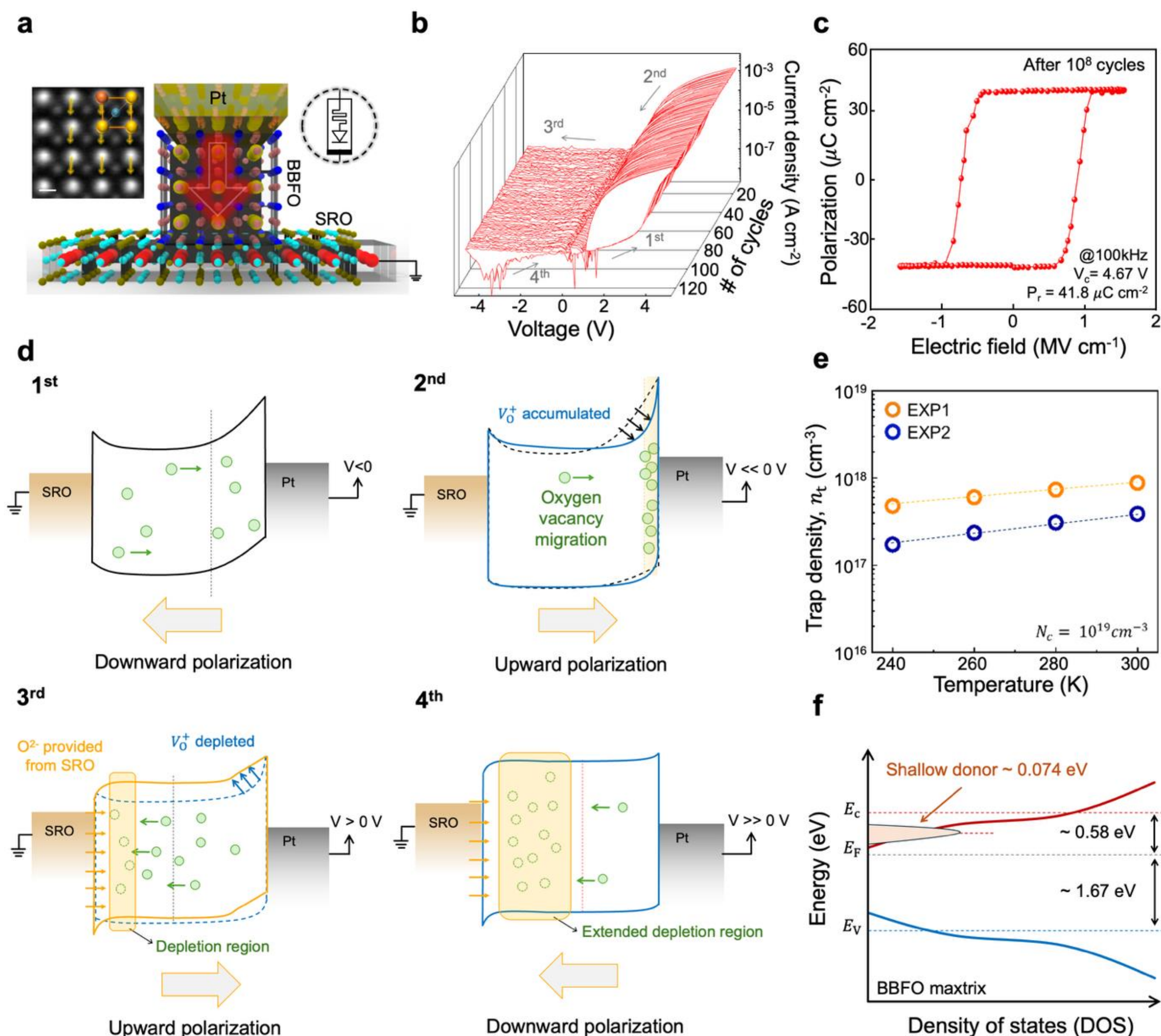

Figure 2. Self-rectifying electrical performance a) Schematic of a unit memristor composed of Pt/BBFO/SRO. The inset shows a STEM-HAADF image of BBFO, with downward arrows indicating the pristine polarization direction. The scale bar is 200pm. **b)** Repetitive J-V cycling measurements using the BBFO memristor, demonstrating stable operation over 100 cycles. The applied voltage was swept from -5 V to 5 V. **c)** Polarization (P) – voltage (V) hysteresis curve measured at 100 kHz for the Pt/BBFO/SRO device. **d)** Evolution of band diagrams illustrating the 4 steps of current transport mechanisms corresponding to the J-V characteristics in Figure 2b. Green circles represent oxygen vacancies, and the arrows in the BBFO band indicate the polarization direction. **e)** Calculated n_t values as a function of temperature based on Table S1 and the following equation, confirming the presence of a donor-like shallow trap state at approximately 0.074 eV. **f)** Energy–density of states diagram constructed based on the band energy analysis.

Electronic-structure calculations based on spin-polarized density functional theory (DFT) were carried out for $Bi_{1-x}Ba_xFeO_3$ with x = 0, ≈ 0.18, and ≈ 0.30, and the density of states (DOS) was quantitatively analyzed in an energy window around the Fermi level (Supplementary figure 20). In that near-E_F region, more than 90% of the states originate from Fe–O networks, whereas the

Ba-projected contribution remains below ~1% and does not form a distinct Ba-centered peak inside the gap, indicating that Ba substitution stabilizes the A-site environment without introducing deep electronic traps and provides an electronically clean ferroelectric matrix within which shallow oxygen-vacancy donors identified by DLTS can modulate conduction. The effect of Ba substitution on rectification behavior was explored by measuring memristive *J-V* characteristics across various Ba concentrations, ranging from 5% to 30% (Supplementary figures 21a-21f). Notably, a high rectifying ratio exceeding 10^5 was only observed when the Ba concentration was 20 %. Ba substitution induces a lattice expansion and optimizes the oxygen-vacancy concentration, thereby mitigating leakage currents and strengthening the diode-like rectifying behavior. [37] In compositions with Ba content deviating from 20 %, suppression of ferroelectric polarization or an increase in oxygen vacancies reduces the rectifying ratio and can even lead to switchable rectifying characteristics. [38] The overall trend indicates that 20 % Ba substitution provides the most suitable composition for fabricating selector-free CBA. Contribution of oxygen vacancy migration to the switching mechanism was indirectly supported by current relaxation behavior under external bias (Supplementary figure 22) and varying ambient temperatures (Supplementary figure 23). Such rectifying behavior was reduced with decreasing BBFO thickness, as shown in Supplementary figures 24a, 24b. This observation suggests that the enhanced diode effect originates from the expansion of ferroelectric domains, which contributes to improved rectification.

Rectifying electrical performances are consistently observed through memristive *J-V* measurements conducted on 25 devices comprehensively over 50 cycles, as shown in Supplementary figure 25. Considering the high device-to-device (D2D) and cycle-to-cycle (C2C) reproducibility observed across 25 memristors, where the rectifying ratio in all graphs exceeds 10^5, BBFO can be considered as a promising memristor material candidate for selector-free CBA

ARTICLE IN PRESS

integration.

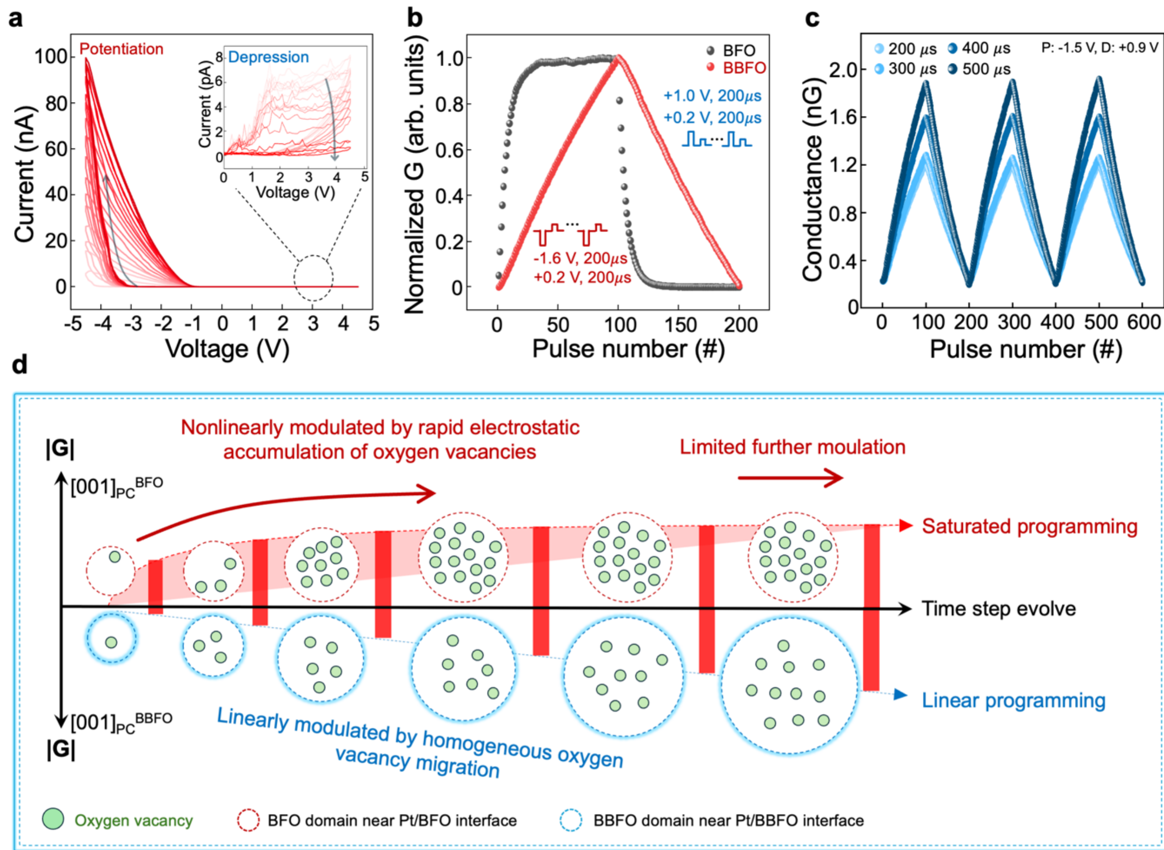

Figure 3. Artificial synapse performances using BBFO memristor a) Analog DC sweeping measurement showing synaptic potentiation and depression over 15 cycles. The inset presents a magnified view of the positive voltage region to highlight the depression characteristics. **b)** Potentiation/depression characteristics measured by 100 pulse number using BFO and BBFO memristors. The applied programming voltages were -1.6 V/+1.0 V, respectively, with a read voltage of +0.2 V. The pulse duration was 200 µs. The nonlinearity at LTP and LTD (v_{po} and v_{de}) was denoted in Figure 2b, as 0.152 and 0.303, respectively. **c)** SWDP characteristics. The voltage amplitudes of the pulses for synaptic weight potentiation and depression are -1.7 V and +1.1 V, respectively. **d)** Illustration of linearity mechanism in the case of BBFO and BFO memristor. The inset image depicts the oxygen vacancy migration influenced by dipole arrangement in the BBFO.

Artificial synapse performances

The synaptic capability of the BBFO memristor was evaluated through an analog DC voltage sweep from -4.5 V to 4.5 V (Figure 3a). The data show that the LRS current level is significantly higher than the HRS level, with a gradual increase in conductance observed in both potentiation

ARTICLE IN PRESS

and depression regions. This consistent conductance modulation in the BBFO memristor is also evident in its long-term potentiation/depression (LTP/LTD) performance (Figure 3b). Notably, the BBFO memristor exhibits much better linearity compared to the BFO memristor in which the nonlinearity values for LTP/LTD are 5.1/5.0 for BFO memristor and 0.152/0.303 for BBFO memristor, respectively. The detailed method for nonlinearity fitting is explained in Supplementary Note 3. The linearity of the BBFO memristor arises from the homogeneous migration of oxygen vacancies, facilitated by the coupling between oxygen vacancy dynamics and ferroelectric conduction, which effectively prevents premature saturation. The fact that the oxygen vacancy can be played as a conduction medium in this study can be evidenced by the change of oxygen concentration in BBFO in XPS depth profiling (Supplementary figures 26a-26b). When applying LTP and LTD voltage pulses, the sharp and gradual decrease in oxygen concentration at Pt/BBFO interface and at throughout BBFO layer can be observed. These observations suggest that the memristive reset characteristics and LTD behavior are primarily governed by a reduction in mobile charge carriers associated with the decrease in oxygen vacancies. During the LTP measurements, the polarization direction remains unchanged due to the insufficient magnitude of the programming voltage, which is lower than the coercive voltage (V_c) in the *P-E* curve of Pt/BBFO/SRO structure (Supplementary figure 6b). However, the migration of oxygen vacancies locally affects the dipole arrangement within BBFO, influencing their velocity. Then, the conductance can be homogeneously controlled across the BBFO energy barrier along with the control of depletion width induced by oxygen vacancy migration (Supplementary figure 27a). Conversely, during the LTD measurements, oxygen vacancies migrate away from the Pt electrode. While the polarization direction remains unchanged still due to the small voltage magnitude lower than V_{oc}, oxygen vacancies begin to be insufficient due to the additional providing of oxygen ions

ARTICLE IN PRESS

ARTICLE IN PRESS

from SRO (Supplementary figure 27b). Contrary to the LTP mechanism, in the case of LTD, the linearity can be explained by the regularly annihilated mobile charges. Considering the results in Supplementary figure 28a showing that the nonlinear behaviors in LTP/LTD induced by the voltage magnitude for the BBFO poling is more degraded as high voltage pulses applied, the assumption that the dipole arrangements by the small voltage pulses within $\pm$ 2V homogeneously change the velocity of oxygen vacancy migration can be persuaded. Also, the fact that the current magnitude in the negative voltage range is higher than that in the positive voltage range considering Figure 2b well corresponds with the higher conductance value after negative poling voltage, as shown in Supplementary figure 28b.

Spike timing dependent plasticity (STDP) measurements reveal a pronounced expansion of the dynamic range for pulse time differences of less than a few milliseconds, as shown in Supplementary figure 29a. The pronounced dynamic range expansion indicates that oxygen vacancy migration induced by Ba alloying effectively captures the temporal correlations between distinct voltage pulses applied at both electrodes on a fast timescale. The mean decay times, fitted for LTD and LTP, are 12.21 ms and 11.49 ms, respectively, while the mean weight change rates are calculated as 148.2% and 145.8% for LTD and LTP, respectively. Paired-pulse facilitation (PPF) measurements (Supplementary figure 29b) indicate that reducing the interval between pulses applied to the device results in a nonlinear enhancement of the dynamic range, allowing sufficient modulation on a timescale of tens to hundreds of microseconds. The PPF ratio was calculated as $\left[\frac{A_2-A_1}{A_1}\right] \times 100\%$. [39] Spike number dependent plasticity (SNDP) characteristics, shown in Supplementary figure 30a, illustrate the effects of a 200 μs pulse train. Despite the limited migration time of oxygen vacancies, high linearity and symmetry are maintained. Spike width

ARTICLE IN PRESS

dependent plasticity (SWDP) and spike voltage dependent plasticity (SVDP) measurements, displayed in Figure 3c and Supplementary figure 30b, demonstrate robust conductance change behaviors, even when the input pulse waveform is varied. Increasing the duration of the input voltage segment affords more time for oxygen vacancies arising from Ba bonding to migrate, thereby inducing conductance modulation over a relatively broader dynamic range. The dynamic range remained comparable between pulse durations of 200 μs and 300 μs, while pulse durations of 400 μs and 500 μs appeared to lead to a noticeable increase. Furthermore, Supplementary figure 30c illustrates spike width–voltage-dependent plasticity (SWVDP), where conductance modulation is examined as a function of pulse duration and voltage magnitude, ranging from 1.3 V to 2.2 V. In the case of SWVDP applied by 1.3 V voltage pulses, prolonged pulsing cannot sustain conductance modulation with showing a conductance saturation when the time duration of voltage pulse was 1.5 ms. In contrast, at 2.2 V, increasing the pulse duration up to 3 ms resulted in uniform resistance modulation. These results suggest that optimizing the timescale can mitigate saturation effects caused by a stronger electric field driving oxygen vacancy migration.

ARTICLE IN PRESS

To determine whether oxygen vacancy migration drives conductance modulation in the BBFO synaptic device, ultrafast pulses were applied, and the corresponding device response was analyzed. As shown in Supplementary figures 31a, 31b, 100 uniform LTP/LTD pulses of 20 ns and 500 ns were applied. A read voltage of 0.1 V was applied between the writing pulses to track conductance states. The dynamic range was significantly smaller at sub-microsecond scales compared to hundreds of microseconds. These findings indicate that oxygen vacancies migrate insufficiently below a few microseconds, resulting in minimal resistance change. Considering the polarization switching response time of BBFO, the conductance modulation observed in our synaptic device suggests that oxygen vacancy migration is the dominant mechanism rather than multilevel

ARTICLE IN PRESS

polarization switching. This robust conduction mechanism by oxygen vacancy migration is also supported by long-term retention measurement, which shows stable conductance level by the time above 5000 seconds (Supplementary figure 32).

As illustrated in Figure 3d, the linearity of BBFO and BFO memristor can be compared based on ferroelectric domain schematics as a function of the number of applied voltage pulses. In the case of BFO memristor, oxygen vacancies are dramatically accumulated due to the strong electrostatic field from pristine ferroelectricity. In contrast, BBFO contains an optimal density of oxygen vacancies in which oxygen vacancy ratio among possible oxygen sites is 7.82 %. This oxygen vacancy ratio isn't high enough to impede ferroelectricity, so the oxygen vacancy can be migrated in the opposite way with maintaining ferroelectricity conditions. At the initial step of voltage pulse application, the oxygen vacancies may be diffused toward the Pt/BBFO interface. As voltage pulses are continuously applied, the initial slow migration of oxygen vacancies can be further accelerated by the electric fields arising from surrounding local dipoles. This process mitigates the initial saturation of vacancy migration, thereby contributing to the linear programming of artificial synapse. The correlation between oxygen vacancy dynamics and ferroelectricity governs both the rectifying J–V characteristics and linear synaptic programming. This interplay is bidirectional, with oxygen vacancy accumulation affecting ferroelectric polarization and, conversely, dipole reorientation influencing vacancy migration. Together, these coupled mechanisms represent key considerations in the design of selector-free CBA materials for reliable neuromorphic hardware.

Relationship between oxygen vacancy migration and ferroelectricity

The influence of oxygen vacancies on ferroelectric behavior has been extensively studied. [40-

ARTICLE IN PRESS

ARTICLE IN PRESS

44] In BBFO, Ba substitution induces oxygen vacancies, but vacancy concentration alone is insufficient for linear resistance modulation. We propose that BBFO's intrinsic ferroelectricity facilitates vacancy migration via internal dipolar fields, enabling the observed linear synaptic behavior. To examine this, we assumed that (1) dipole alignment responds dynamically to vacancy migration, and (2) mobile oxygen vacancies interact electrostatically with surrounding local dipoles, modulating the migration barrier. As illustrated in Supplementary figures 2a-2c, Bi and Ba share the A-site position, supporting the view that vacancy formation and dipole generation are complementary. We examined their interplay by analyzing (1) vacancy migration relative to dipole displacement, and (2) polarization response with respect to the degree of vacancy migration. The results support a second-order mechanism in BBFO, in which polarization and oxygen vacancy migration act as coupled internal variables, and device operation arises from their interdependent dynamics rather than from a single dominant process. [45-47]. In contrast, single-process-dominated behavior, as commonly observed in interface-type and filamentary-type switching, leads to progressive insensitivity and saturation of conductance modulation due to the accumulation of responses under repeated stimuli. This coupled evolution of ferroelectric polarization and oxygen vacancy migration gives rise to the second-order switching mechanism, as depicted in Supplementary figure 33.

First, the dipole response under varying degrees of potentiation and depression was assessed using positive-up-negative-down (PUND) measurements at 4 kHz triangular 8 V pulses. As shown in Supplementary figures 34a, 34b, the polarization response decreased after LTP and recovered during LTD. This behavior can be attributed to two effects: (1) vacancy migration toward the Pt electrode reduces electric field strength, weakening dipole switching response; and (2) redistribution toward the SRO side allows oxygen compensation, restoring polarization response.

ARTICLE IN PRESS

ARTICLE IN PRESS

This interpretation is supported by the *J–V* characteristics, while the minimal variation in leakage current during U and D pulses confirms that the transient current changes originate from reversible dipole activity governed by oxygen vacancy distribution, rather than increased leakage.

Second, we investigated the influence of local dipole states on vacancy migration using two pulse schemes: short triangular pulses (<5 μs) for dipole alignment and longer rectangular pulses (~200 μs) for vacancy modulation. Four poling-response conditions were tested following vacancy initialization. As shown in Supplementary figure 35, stronger negative poling (−5 V to −7 V) facilitated vacancy migration and increased conductance, while positive poling suppressed modulation. Devices subjected to stronger prior negative poling exhibited lower resistance under the same +5 V bias, indicating that residual dipolar fields persist and continue to influence vacancy transport. These findings underscore the role of dipole realignment in regulating vacancy dynamics during synaptic operation.

Finally, we examined dynamic interactions between migrating oxygen vacancies and adjacent local dipoles during synaptic programming. In LTP and LTD operations involving repeated unipolar pulses, both vacancy migration and gradual dipole alignment are expected. To investigate these effects, we similarly applied separate dipole-control and vacancy-control pulses under incrementally increasing poling voltages (+5 V to +9 V). Each time the dipole state was changed, we performed five LTD learning steps, followed by a single LTP pulse, and observed the resulting resistance changes. Supplementary figure 36 shows the voltage schemes and LTP current responses. The current baseline during LTP pulsing decreased progressively with gradually increasing dipole alignment. In contrast, when strong poling was applied first and then reduced in same direction, resistance changes were minimal. These results imply that the dynamically

ARTICLE IN PRESS

ARTICLE IN PRESS

changing dipole environment contributes to the uniform migration of oxygen vacancies by controlling the energy barrier for vacancy migration, which in turn aids linear resistance modulation. This coupled mechanism between dipoles and vacancies may be critical for reliable synaptic programming with repeated unidirectional pulses (see Supplementary figures 37-39). A detailed investigation of the measurement methodology and the underlying mechanisms is provided in Supplementary Notes 4 and 5.

From our measurements, two key conclusions can be drawn: (1) Ba-induced oxygen vacancies affect dipole alignment, and (2) vacancy migration is modulated by the extent of dipole ordering. Supplementary figure 40 illustrates this coupling during synaptic operation. Under a ferroelectric polarization environment, the velocity of oxygen vacancies varies with the number of applied voltage pulses. Although the pulse amplitude remains below V_c, repeated subthreshold pulses (±2 V) can gradually tilt the dipole configuration, which in turn promotes the otherwise delayed migration of oxygen vacancies. During programming, vacancies dynamically interact with local dipoles near Ba/Bi cations, modifying the polarization state. While the vacancy-control pulses alone are insufficient to induce complete polarization switching, the progressive dipole alignment compensates for the delayed vacancy migration, thereby preventing early saturation. These dynamics differ slightly between LTP and LTD processes. In LTP, migration is initially hindered by oppositely oriented dipoles but becomes facilitated as polarization aligns and the internal field increases. In LTD, vacancy annihilation near the SRO interface and dipole recovery suppresses initial migration and reduces the risk of saturation over successive cycles. Such dynamic coupling prevents premature saturation and enables linear modulation of resistance, indicating the presence of a second-order feedback mechanism between dipole orientation and vacancy distribution.

ARTICLE IN PRESS

Endurable synaptic weight update

The BBFO memristor demonstrates robust synaptic performance across various input pulse waveforms, ensuring stable characteristics over extended cycling. This durability is crucial for achieving durable resistance modulation in forming free memristive synapse devices at the chip scale**.** Cycle endurance measurements**,** shown in Figure 4a, were conducted by applying 400 potentiation and 400 depression pulses, each with a voltage pulse duration of 200 μs. Even after 10 million pulses, the conductance modulation remained stable without any electrical degradation across all cycling (Supplementary figure 41). These endurable performances may be attributed to non-scattering charge modulation due to epitaxially grown-BBFO and to the reproducible interactive effect between ferroelectricity and oxygen vacancies.

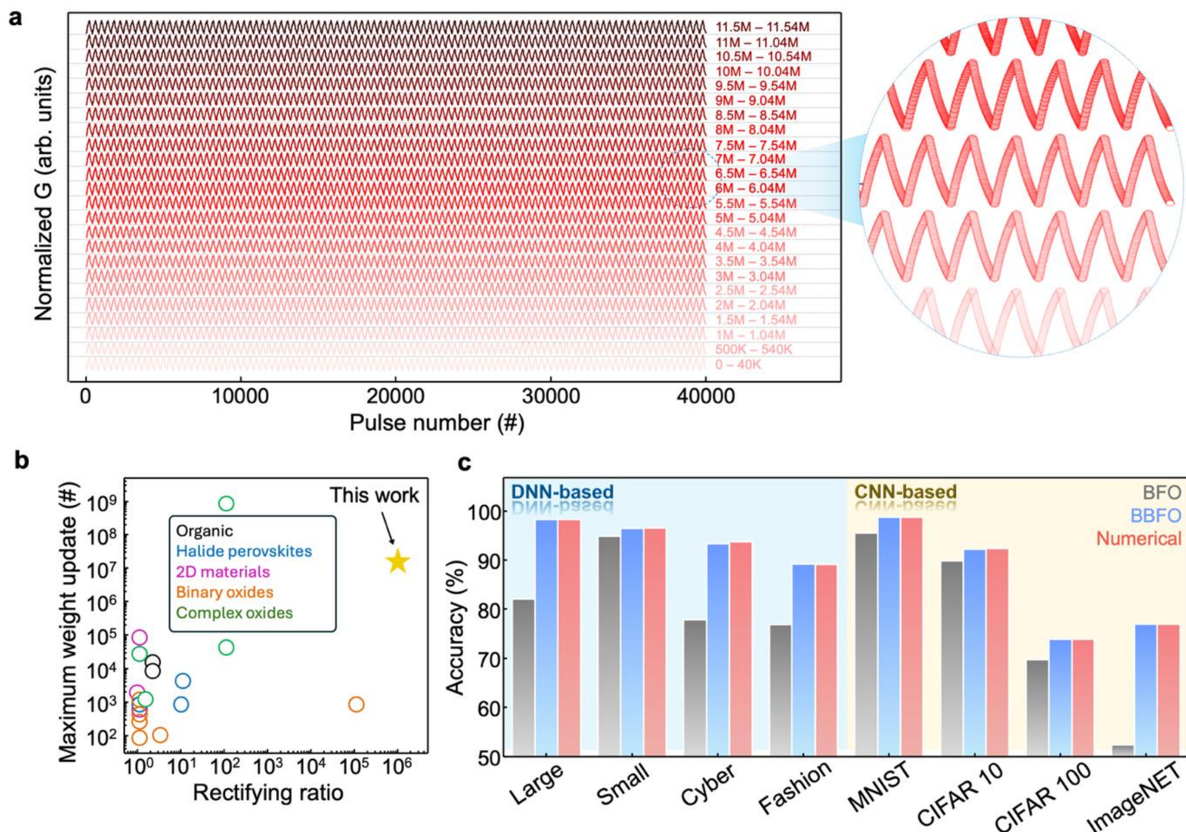

Figure 4. **Endurable artificial synaptic performance and training results using the BBFO memristor**. **a)** Cycle

ARTICLE IN PRESS

endurance measurements for LTP/LTD, with 400 pulses applied for each. **b)** Comparison of rectification and state-update endurance between the BBFO device and other memristor-based artificial synaptic devices. **c)** Deep learning simulation results comparing training accuracy for BFO and BBFO synaptic devices. The blue region represents DNN-based training, the yellow region corresponds to CNN-based training, and the purple line indicates numerical training results.

The robustness of the BBFO synaptic device under high-temperature conditions is presented in Supplementary figures 42a, 42b. The potential influence of heat generation during device operation on reliability was examined through cycle endurance measurements at 473 K, with a voltage time duration of 200 μs and 400 voltage pulses applied for LTP/LTD measurements. These results confirm stable performance even after 10 million pulses. However, at elevated temperatures, conductance modulation became more nonlinear and asymmetric, possibly due to enhanced thermal activation of oxygen vacancy migration leading to earlier saturation (Supplementary figure 42c). These findings further support oxygen vacancy migration as the primary mechanism governing resistance modulation in BBFO synaptic devices.

ARTICLE IN PRESS

The quantitative comparison of rectification and state-update endurance for the BBFO memristor, benchmarked against artificial synaptic devices based on organic compounds, halide perovskites, 2D materials, binary oxides, and complex oxides, is graphically illustrated in Figure 4b. This analysis is derived from the broader comparative study presented in Supplementary Table 2, which compiles performance metrics from previous studies. [12, 15, 39, 48-63] Expected performance metrics for BBFO synaptic devices in CBAs designed for deep learning accelerators are depicted in Figure 4c. In BFO, ferroelectric polarization acts as the major conduction medium, making conduction modulation difficult to be linear. As a result, the training accuracy is significantly lower than the numerical computation results. This discrepancy suggests difficulties in precisely regulating feedback mechanisms needed to compensate for nonlinear and asymmetric resistance modulation, including pulse train characteristics (e.g., pulse count and voltage

ARTICLE IN PRESS

magnitude). In contrast, simulations of a MAC accelerator using BBFO devices result in closer alignment with numerical outcomes due to more consistent and linear conductance modulation. These findings suggest that BBFO thin films can support effective learning when integrated into chip-scale neuromorphic hardware. Simulations of CNN-based computations further indicate broad applicability in neural networks requiring MAC operations. Neural network architectures and learning outcomes are illustrated in Supplementary figures 43–45 and Supplementary Table 3.

Implementation of selector-free crossbar arrays using $Bi_{0.8}Ba_{0.2}FeO_3$

We demonstrated the feasibility of implementing high-rectification synaptic devices using epitaxially grown ferroelectric BBFO single thin films. A CBA system aligned with the device structure was fabricated to verify the practical applicability of this approach. A schematic representation of the 11 × 11 CBA developed in this study is provided in Figure 5a, highlighting its structural organization and key functional components. The width of each line pattern was designed to match the 50 μm × 50 μm square area of the characterized device. If each cell in the CBA maintains rectification and linear conductance modulation, it would be possible to develop a neuromorphic computing system that is robust against external interference. For bit-line integration, we etched an SRO (001) thin film to form the bitlines while carefully controlling the (001) surface to ensure that BBFO could still grow epitaxially following the orientation of SRO.

ARTICLE IN PRESS

Elemental distribution and crystalline quality of BBFO films grown on etched SRO bitlines are examined using EDS and EBSD, as shown in Supplementary figures 46a, 46b. The EDS elemental mapping clearly distinguishes the SRO line pattern, confirming its distinct separation. Additionally, the EBSD analysis indicates that BBFO continues to grow as an epitaxial single-phase thin film, maintaining its (001) orientation, guided by the line patterned SRO seed and surrounding STO

ARTICLE IN PRESS

(001) substrate. Supplementary figures 47a-47f provides the etched SRO information including etching images and *J*-*V* curves to show electrical isolation from another adjacent SRO line. This huge resistance between the two adjacent SRO electrodes (3.3 GΩ) alludes that the SRO bitline design prevents unintended conductive paths toward neighboring cells. Despite ex-situ deposition, BBFO maintains epitaxial growth even after etching the SRO into a line pattern, as demonstrated in Supplementary figure 48a. The OM images after depositing BBFO at overall substrate (Supplementary figures 48b-48d) further validate the structural integrity of SRO bitlines and BBFO film.

As shown in Figure 5b, we patterned the top wordline Pt electrodes to construct an 11 × 11 CBA. Elemental differentiation of the CBA, confirmed by EDS mapping, is globally presented in Supplementary figure 49. Using this CBA structure, we can successfully suppress the unwanted parasitic current path during the potentiation and depression process (Figure 5c) within a full substrate. Thanks to these self-rectifying performances using the uniform BBFO film, LTP and LTD characteristics across all 121 cells in the 11 × 11 CBA demonstrate highly linear conductance modulation with minimal variation (Figure 5d). Supplementary figure 50 quantitatively presents statistical information on the LTP/LTD characteristics of each cell within the 11 × 11 CBA, including the 95% confidence intervals and deviations. *J*-*V* characteristics of individual cells in the CBA are also shown in Figure 5e and Supplementary figure 51, highlighting D2D uniformity and operational stability. The results reveal a uniform memory window exceeding two orders of magnitude and a rectification ratio exceeding six orders of magnitude across the entire array. The use of non-identical LTP/LTD voltages originates from differences in the effective electric field required for comparable resistance modulation, arising from the asymmetric device configuration, including work-function mismatch, remanent polarization, and the resulting built-in electric field.

ARTICLE IN PRESS

ARTICLE IN PRESS

Consequently, different voltage amplitudes are required for LTP and LTD. Consistent with this mechanism, although the dot-patterned cells in Figure 1f require different absolute voltages, the same positive-to-negative voltage ratio produces comparable synaptic behavior, confirming the validity of the proposed device mechanism in the CBA architecture. The high rectification ensures reliable readout during synaptic weight modulation and retention, reinforcing the stability of the CBA. Additionally, the uniformity of individual cells suggests the potential for scaling the array to larger sizes.

ARTICLE IN PRESS

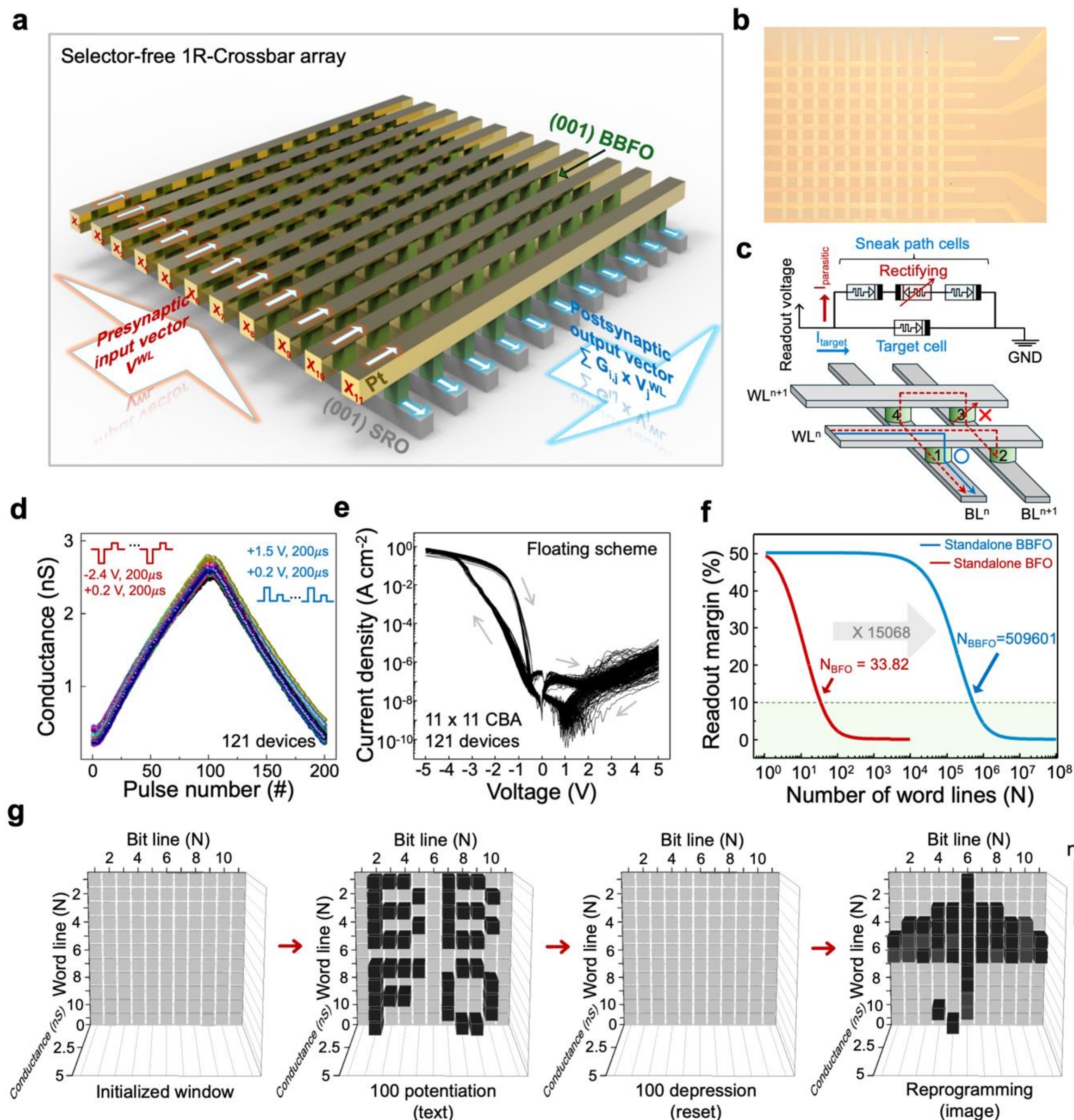

Figure 5. Implementation of the 11×11 BBFO selector-free crossbar array. **a)** Schematic of the selector-free BBFO CBA. **b)** Optical microscope image of the fabricated CBA. The scale bar is 200 μm. **c)** The sneak current blocking mechanism of self-rectifying memristors during CBA operation. Red-colored devices represent reverse-biased elements, blue-colored devices indicate forward-biased elements, and white-colored devices correspond to target cells. **d)** LTP/LTD characteristics of individual CBA cells, with applied pulses of -2.4 V and +1.5 V, respectively. In all cases, the read voltage was +0.2 V, and the pulse duration was 200 μs. **e)** *J-V* measurement results for individual cells within the CBA. **f)** Read margin comparison of selector-free CBAs based on BBFO and BFO. The blue line represents BBFO, while the red line corresponds to BFO. **g)** Learning demonstration results using the 11×11 BBFO CBA.

A comparative analysis of read margin performance between CBAs composed of BFO and BBFO is shown in Figure 5f, demonstrating the advantages of BBFO in maintaining stable and

ARTICLE IN PRESS

distinguishable conductance states. Within the circuit's error tolerance range, the BBFO CBA exhibits a size scalability over 15,000 times greater than the conventional BFO-based array, making it highly promising for integrated neuromorphic systems. This high read margin is attributed that Ba alloying enables optimizing CBA integration, including leakage current suppression, controllable vacancy migration under strong ferroelectricity conditions. The influence of the rectification ratio of self-rectifying memristors on CBA operation and the calculation method are detailed in Supplementary Note 6. Our BBFO memristor allows a maximum array size accommodating 260G cells under the 10% readout margin criterion. As shown in Figure 5g, experimental validation confirms the feasibility of text programming in the BBFO CBA, demonstrating that stored states can be erased and retrained with different images. The high rectification enables that voltage application during array-level measurements did not significantly affect device operation. The applied voltage selectively potentiated target cells, enabling the learning of text and image patterns. Additionally, the array could be successfully reset by applying a depression pulse sequence equal in number to the previously applied potentiation pulses due to the linear and symmetric potentiation and depression characteristics. The ability to train on various types of data aligns with the earlier DNN and CNN simulation results, which is likely due to the high rectification and the capability for linear, symmetric resistance modulation. Operational principles of the CBA, emphasizing the advantages of selectively programming individual cells, are detailed in Supplementary figures 52a-52e. In circuitry perspectives, sneak paths correspond to leakage currents through neighboring cells, forming an equivalent circuit model. Since at least one reverse-biased BBFO memristor exists within each sneak path, the high rectification of BBFO effectively suppresses leakage currents, ensuring that only the intended data is programmed into the array.

ARTICLE IN PRESS

ARTICLE IN PRESS

ARTICLE IN PRESS

ARTICLE IN PRESS

Discussion

We present BBFO memristor, fabricated by incorporating 20 % Ba into BFO within a Pt/BBFO/SRO structure. The electrical behavior of the BBFO memristor is governed by a strong coupling between ferroelectric polarization and oxygen vacancy dynamics, enabling a high rectifying ratio through reliable modulation of the energy barrier. This mechanism also enables stable and linear modulation of synaptic weights, as consistent oxygen vacancy migration—regulated by the number of applied voltage pulses and influenced by local dipolar fields—allows for reliable programming of LTP/LTD characteristics. These properties contribute to circuit-level advantages for stable CBA operation. Furthermore, the defect-free interface formed by epitaxial growth ensures excellent endurance, with the device maintaining performance even after 10 million LTP/LTD cycles. These findings suggest that second-order control of polarization-assisted vacancy migration provides a distinctive mechanism for nonvolatile memory functionality, while effectively suppressing the intrinsic leakage pathways associated with the original BFO framework. Owing to the favorable electrical properties that support CBA integration and synaptic functionality, we successfully fabricated an epitaxially grown BBFO-based CBA without the need for additional selector elements. The 11 × 11 array exhibited negligible D2D variability, with less than 1 % variation in the on/off current ratio among 121 devices, highlighting the potential of BBFO for reliable and uniform neuromorphic hardware implementation. These results indicate that BBFO-based mechanism can underpin practical CBA realization in future IMC systems. As wafer-scale epitaxy and epitaxial transfer continue to mature, the device-operation mechanism has strong potential for practical, large-scale integration in future neuromorphic hardware platforms.

ARTICLE IN PRESS

ARTICLE IN PRESS

Methods

Fabrication of $Bi_{1-x}Ba_xFeO_3$ ceramic targets

Pure $BiFeO_3$ and Ba doped $BiFeO_3$ ceramic targets were prepared using conventional solid-state reaction method. $Bi_{1-x}Ba_xFeO_3$ (x = 0, 0.05, 0.1, 0.15, 0.2, 0.25, 0.3) weighed following stoichiometric amounts of Bi_2O_3 (99.99%, High Purity Chemicals), $BaCO_3$ (99.95%, Alfa Aesar), and Fe_2O_3 (99.9%, High Purity Chemicals) and thoroughly mixed using ball milling for 24 hours. The mixed powders were subsequently calcined at 800 °C for 5 hours and hand ground with a mortar and pestle. The synthesized powders were pressed into pellets and subsequently sintered. The temperature was maintained at 700°C for 30 minutes, then gradually increased to 800°C over 30 minutes, followed by sintering at 800°C for 12 hours.

ARTICLE IN PRESS

Growth of epitaxial $Bi_{1-x}Ba_xFeO_3/SrRuO_3$ thin films

The epitaxial $Bi_{1-x}Ba_xFeO_3/SrRuO_3$ (x = 0, 0.05, 0.1, 0.15, 0.2) thin films were deposited on (001) $SrTiO_3$ single crystal substrate (Crystal, Gmbh) through pulsed laser deposition (PLD) using KrF 248 nm excimer laser (COHERENT, COMPEX PRO 205F). The film thickness of BFO and SRO were 100 and 40 nm, respectively. Under an oxygen partial pressure of 100 mTorr, the SRO thin film was first deposited with a laser with 3 Hz repetition, 2.0 Jcm^{-2} energy density at 680 °C, whereas the pure $BiFeO_3$ and Ba doped $BiFeO_3$ thin films were deposited under an oxygen partial pressure of 200 mTorr, with a laser of 10 Hz repetition, 2.0 Jcm^{-2} energy density at 670 °C. The target-to-substrate distance of 50 mm was employed for all layers. The deposited film was cooled at a rate of 30°C per minute under an oxygen pressure of 50 Torr. The Pt TEs were deposited using E-beam evaporator (SRN-200, SORONA). The size of Pt TEs was 50×50 μm^2, and these TE patterns could be realized using chromium shadow mask. For CBA fabrication, we patterned and

ARTICLE IN PRESS

wet-etched the SRO thin film into bit lines using a standard lithography process. For selective etching of the SRO layer, an aqueous 0.4 mol/L sodium metaperiodate ($NaIO_4$) solution was prepared and sonicated for 30 min to ensure complete dissolution. The SRO film patterned with photoresist was then immersed in the solution for 30 s to remove the exposed SRO. After stripping the photoresist, the BFO layer was subsequently deposited ex-situ under the conditions described above. followed by the patterning of the top cross-line electrodes using the lift-off process.

Material Characterizations

The crystal structure of BBFO/SRO film was investigated by theta-2theta XRD (Bruker, D8 Discover), XRC, phi-scan, and RSM (PANalytical, Xpert Pro) with Cu Kα radiation (λ = 1.5418 Å). XRD PDF card numbers for BBFO, SRO, and STO were 04-019-6114, 01-072-5834, and 00-005-0634, respectively. OM image of the device was obtained from an optical microscopy (Leica Microsystems CNS GmbH, DM4000 M LED). Out-of-plane Piezoresponse force microscope (PFM) measurements were performed using a Bruker Dimension Icon. The Pt/Ir coated tip (SCM-PIT V2) with a spring constant (k) of ~3 N m^{-1} and a resonant frequency of ~75 kHz was employed. In contact mode, an AC voltage at 25 kHz was applied between the conductive probe and grounded sample. This frequency is well below the resonance frequency of the cantilever and contact resonance of the tip–sample system to avoid artificial amplification of the signal. Cross-sectional STEM images in low magnitude and HAADF version were obtained (Themis Z, ThermoFisher) after focusing ion beam (FIB) sampling (SMI3050Sem SII Nanotechnology). UPS measurements were obtained using a ThermoFisher Scientific NEXSA G2 XPS system calibrated with Au standards. X-ray photoelectron spectroscopy (Thermo Scientific, ESCALAB 250Xi) was

ARTICLE IN PRESS

ARTICLE IN PRESS

utilized to verify the Co oxidation state and depth profile. All spectral peaks were calibrated using the carbon 1s peak as a reference.

Electrical Characterizations

Consecutive memristive *J–V* curves, analog sweep curves, and cell-to-cell variability were obtained using a 4-tip probe station (MSTECH, Agilent 4156C). DC voltage sweeps were applied to the top electrode while the bottom electrode was grounded. The *J–V* sweeps were performed in a dual-sweep manner, from 0 to -5 V and from 0 to 5 V, with a sweep velocity of 0.2 Vs^{-1}. The SRO electrode was kept at ground potential during the measurements. Analog sweeps were conducted by applying 15 consecutive sweeps from 0 to -4.5 V, followed by 15 sweeps from 0 to 4.5 V at the same sweep velocity. The P-E curve and the polarization endurance was characterized by a 4-tip probe station (Keithley, 4200A-SCS) equipped with a polarization measurement program (RADIANT Technologies. InC., Precision LC Ferroelectric Tester). Synaptic electrical characteristics, including multi-level retention and endurance, were measured using a 4-tip probe station (Keithley 4200A Semiconductor Analyzer and Keithley 2636A). The probe tip diameter used for all electrical measurements was 30 μm. DLTS measurement was conducted using a Keithley 4200A-SCS equipped with a capacitance measurement unit (CMU) under conditions employed by an oscillation level of 25 mV and a frequency of 10 kHz.

ARTICLE IN PRESS

Computational details

All the spin-polarized density functional theory (DFT) calculations were performed using the Vienna Ab initio Simulation Package (VASP) program with the projector augmented wave method for the core region and a plane-wave kinetic energy cutoff of 400 eV. The generalized gradient

ARTICLE IN PRESS

approximation (GGA), in the form of Perdew-Burke-Ernzerhof (PBE), was used for the exchange-correlation potentials. A 4x4x1 Gamma-centered Monkhorst-pack sampled k-point grid was employed to sample the reciprocal space. The atoms are free to move in all directions until the convergence of energy and residual atomic force on each atom was less than $1x10^{-4}$ eV and 0.01 eV/Å, respectively.

Data Availability

The data that support the conclusions of this study are available from the corresponding authors upon request.

Code Availability

The code that used for the software simulation for this study is available from the corresponding authors upon request.

ARTICLE IN PRESS

ARTICLE IN PRESS

References

1. Merolla, P.A., et al., A million spiking-neuron integrated circuit with a scalable communication network and interface. *Science*, 2014. **345**(6197): p. 668-673.
2. Mayberry, M., Intel's new self-learning chip promises to accelerate artificial intelligence. *Intel* (25 September 2017), 2017.
3. Imam, N. and T.A. Cleland, Rapid online learning and robust recall in a neuromorphic olfactory circuit. *Nature Machine Intelligence*, 2020. **2**(3): p. 181-191.
4. Kim, Y., C.W. Lee, and H.W. Jang, Neuromorphic Hardware for Artificial Sensory Systems: A Review. *Journal of Electronic Materials*, 2025: p. 1-42.
5. Yang, J.J., et al., Memristive switching mechanism for metal/oxide/metal nanodevices. *Nature nanotechnology*, 2008. **3**(7): p. 429-433.
6. Rao, M., et al., Thousands of conductance levels in memristors integrated on CMOS. *Nature*, 2023. **615**(7954): p. 823-829.
7. Song, W., et al., Programming memristor arrays with arbitrarily high precision for analog computing. *Science*, 2024. **383**(6685): p. 903-910.
8. Yang, J.J., D.B. Strukov, and D.R. Stewart, Memristive devices for computing. *Nature nanotechnology*, 2013. **8**(1): p. 13-24.
9. Chen, S., et al., Electrochemical-memristor-based artificial neurons and synapses—fundamentals, applications, and challenges. *Advanced materials*, 2023. **35**(37): p. 2301924.
10. *INTERNATIONAL ROADMAP FOR DEVICES AND SYSTEMS 2023 UPDATE BEYOND CMOS THE IRDS IS DEVISED AND INTENDED FOR TECHNOLOGY ASSESSMENT ONLY AND IS WITHOUT REGARD TO ANY.* 2023.
11. Kim, S.J., et al., Vertically aligned two-dimensional halide perovskites for reliably operable artificial synapses. *Materials Today*, 2022. **52**: p. 19-30.
12. Kwak, K.J., et al., Ambient stable all inorganic $CsCu_2I_3$ artificial synapses for neurocomputing. *Nano Letters*, 2022. **22**(14): p. 6010-6017.
13. Im, I.H., et al., Halide perovskites-based diffusive memristors for artificial mechano-nociceptive system. *Advanced Materials*, 2024. **36**(1): p. 2307334.
14. Lee, Y.J., et al., Nanoelectronics using metal–insulator transition. *Advanced Materials*, 2024. **36**(5): p. 2305353.
15. Lee, Y.J., et al., Memristive Artificial Synapses Based on Brownmillerite for Endurable Weight Modulation. *Small*, 2025. **21**(1): p. 2405749.
16. Khasanov, D. and O. Primqulov. Gradient descent in machine learning. in 2021 International Conference on Information Science and Communications Technologies (ICISCT). 2021. *IEEE*.
17. Van Doremaele, E.R., et al., Hardware implementation of backpropagation using progressive gradient descent for in situ training of multilayer neural networks. *Science Advances,* 2024. **10**(28): p. eado8999.
18. Kim, K.S., et al., The future of two-dimensional semiconductors beyond Moore's law. *Nature Nanotechnology*, 2024. **19**(7): p. 895-906.
19. Kim, Y. and H.W. Jang, Designing Memristive Materials for Artificial Dynamic Intelligence. *Advanced Intelligent Discovery*, 2025: p. 202500020.
20. Wang, S., et al., Memristor-based intelligent human-like neural computing. *Advanced Electronic Materials*, 2023. **9**(1): p. 2200877.
21. Xiao, Z., et al., Adapting magnetoresistive memory devices for accurate and on-chip-training-free in-memory computing. *Science Advances*, 2024. **10**(38): p. eadp3710.
22. Jacobs-Gedrim, R.B., et al. Impact of linearity and write noise of analog resistive memory devices in a neural algorithm accelerator. in *2017 IEEE International Conference on Rebooting Computing (ICRC)*. 2017. IEEE.
23. Ren, S.G., et al., Self-rectifying memristors for three-dimensional in-memory computing. *Advanced Materials*, 2024. **36**(4): p. 2307218.
24. Song, M.-K., et al., Recent advances and future prospects for memristive materials, devices, and systems. *ACS nano*, 2023. **17**(13): p. 11994-12039.
25. Wang, Z., et al., High-performance CMOS-compatible self-rectifying memristor for passive array integration. *Physical Review Applied*, 2024. **22**(6): p. 064003.

ARTICLE IN PRESS

ARTICLE IN PRESS

26. Zhang, G., et al., Self-rectifying memristors with high rectification ratio for attack-resilient autonomous driving systems. *Nature Communications*, 2025. **16**(1): p. 5759.
27. Jeong, H., et al., Self-supervised video processing with self-calibration on an analogue computing platform based on a selector-less memristor array. *Nature Electronics*, 2025. **8**(2): p. 168-178.
28. Zhang, G., et al., Self-rectifying memristor-based reservoir computing for real-time intrusion detection in cybersecurity. *Nano Letters*, 2024. **24**(49): p. 15707-15715.
29. Zhang, G., et al., Self-rectifying memristors with high rectification ratio and dynamic linearity for in-memory computing. *Applied Physics Letters*, 2024. **125**(13).
30. Zhang, G., et al., Stochastic self-rectifying memristor crossbar array as physical unclonable function for authentication and tamper-evident image security. *Device*, 2025.
31. Fan, X., et al., Superior rectification self-rectifying memristors with self-recovery capabilities enabled by GaO_x/InO_x heterostructures. *Applied Physics Letters*, 2025. **127**(19).
32. Nian, Y., et al., Evidence for an oxygen diffusion model for the electric pulse induced resistance change effect in transition-metal oxides. *Physical review letters,* 2007. **98**(14): p. 146403.
33. Yang, Q., et al., Strain effects on formation and migration energies of oxygen vacancy in perovskite ferroelectrics: A first-principles study. *Journal of Applied Physics*, 2013. **113**(18).
34. Xiang, X., et al., Manipulating the resistive switching in epitaxial $SrCoO_{2.5}$ thin-film-based memristors by strain engineering. *ACS Applied Electronic Materials,* 2022. **4**(6): p. 2729-2738.
35. Miot, C., et al., X-ray photoelectron spectroscopy characterization of barium titanate ceramics prepared by the citric route. Residual carbon study. *Journal of materials research*, 1997. **12**(9): p. 2388-2392.
36. Yaakob, M., et al., Self-interaction corrected LDA+U investigations of $BiFeO_3$ properties: plane-wave pseudopotential method. *Materials Research Express*, 2015. **2**(11): p. 116101.
37. Lee, D., et al., Polarity control of carrier injection at ferroelectric/metal interfaces for electrically switchable diode and photovoltaic effects. *Physical Review B—Condensed Matter and Materials Physics*, 2011. **84**(12): p. 125305.
38. Liang, N., et al., *Structure evolution and energy band modulation in Ba-doped $BiFeO_3$ thin films.* Journal of Applied Physics, 2024. **135**(4).
39. Kim, S.J., et al., *Linearly programmable two-dimensional halide perovskite memristor arrays for neuromorphic computing.* Nature Nanotechnology, 2025. **20**(1): p. 83-92.
40. Lee, J., et al., *Role of oxygen vacancies in ferroelectric or resistive switching hafnium oxide.* Nano Convergence, 2023. **10**(1): p. 55.
41. Noguchi, Y., et al., *Ferroelectrics with a controlled oxygen-vacancy distribution by design.* Scientific reports, 2019. **9**(1): p. 4225.
42. Kelley, K.P., et al., *Oxygen vacancy injection as a pathway to enhancing electromechanical response in ferroelectrics.* Advanced Materials, 2022. **34**(2): p. 2106426.
43. Scott, J. and M. Dawber, *Oxygen-vacancy ordering as a fatigue mechanism in perovskite ferroelectrics.* Applied Physics Letters, 2000. **76**(25): p. 3801.
44. Li, W., et al., *Correlation among oxygen vacancies in bismuth titanate ferroelectric ceramics.* Applied physics letters, 2004. **85**(20): p. 4717-4719.
45. Mikheev, V., et al., *Ferroelectric second-order memristor.* ACS applied materials & interfaces, 2019. **11**(35): p. 32108-32114.
46. Kim, S., et al., *Experimental demonstration of a second-order memristor and its ability to biorealistically implement synaptic plasticity.* Nano letters, 2015. **15**(3): p. 2203-2211.
47. Kumar, S., et al., *Dynamical memristors for higher-complexity neuromorphic computing.* Nature Reviews Materials, 2022. **7**(7): p. 575-591.
48. Zhong, Y.N., et al., *Synapse-like organic thin film memristors.* Advanced Functional Materials, 2018. **28**(22): p. 1800854.
49. Zhou, J., et al., *A monochloro copper phthalocyanine memristor with high-temperature resilience for electronic synapse applications.* Advanced Materials, 2021. **33**(5): p. 2006201.
50. Li, J., et al., *Polymeric memristor based artificial synapses with ultra-wide operating temperature.* Advanced Materials, 2023. **35**(23): p. 2209728.
51. Lao, J., et al., *An air-stable artificial synapse based on a lead-free double perovskite $Cs_2AgBiBr_6$ film for neuromorphic computing.* Journal of Materials Chemistry C, 2021. **9**(17): p. 5706-5712.
52. Tang, J., et al., *A reliable all-2D materials artificial synapse for high energy-efficient neuromorphic computing.* Advanced Functional Materials, 2021. **31**(27): p. 2011083.

ARTICLE IN PRESS

ARTICLE IN PRESS

53. Shi, Y., et al., *Electronic synapses made of layered two-dimensional materials.* Nature Electronics, 2018. **1**(8): p. 458-465.
54. Yang, J., et al., *Wafer-Scale Memristor Array Based on Aligned Grain Boundaries of 2D Molybdenum Ditelluride for Application to Artificial Synapses.* Advanced Functional Materials, 2024. **34**(15): p. 2309455.
55. Choi, S., et al., *Experimental demonstration of feature extraction and dimensionality reduction using memristor networks.* Nano letters, 2017. **17**(5): p. 3113-3118.
56. Chen, J., et al., *Reconfigurable Ag/HfO_2/NiO/Pt memristors with stable synchronous synaptic and neuronal functions for renewable homogeneous neuromorphic computing system.* Nano Letters, 2024. **24**(17): p. 5371-5378.
57. Peng, Z., et al., *HfO2-based memristor as an artificial synapse for neuromorphic computing with tri-layer HfO_2/$BiFeO_3$/HfO_2 design.* Advanced Functional Materials, 2021. **31**(48): p. 2107131.
58. Park, T., et al., *Au-Nanodots Embedded Self-Rectifying Analog Charge Trap Memristor with Modified Bias Voltage Application Method for Stable Multi-Bit Hardware-Based Neural Network.* Advanced Materials Technologies, 2025: p. 2400965.
59. Sun, Y., et al., *A Ti/AlO_x/TaO_x/Pt analog synapse for memristive neural network.* IEEE Electron Device Letters, 2018. **39**(9): p. 1298-1301.
60. Deng, S., et al., *Selective area doping for Mott neuromorphic electronics.* Science Advances, 2023. **9**(11): p. eade4838.
61. Luo, Z., et al., *High-precision and linear weight updates by subnanosecond pulses in ferroelectric tunnel junction for neuro-inspired computing.* Nature communications, 2022. **13**(1): p. 699.
62. Liu, G., et al., *Silicon based $Bi_{0.9}La_{0.1}FeO_3$ ferroelectric tunnel junction memristor for convolutional neural network application.* Nanoscale, 2023. **15**(31): p. 13009-13017.
63. Moon, K., et al., *Bidirectional non-filamentary RRAM as an analog neuromorphic synapse, Part I: Al/Mo/$Pr_{0.7}Ca_{0.3}MnO_3$ material improvements and device measurements.* IEEE Journal of the Electron Devices Society, 2017. **6**: p. 146-155.

ARTICLE IN PRESS

ARTICLE IN PRESS

Acknowledgements

This research was supported by the Nano & Material Technology Development Program through the National Research Foundation of Korea (NRF) funded by the Ministry of Science and ICT (RS-2024-00450836). This work was also supported by the National Research Foundation of Korea (NRF) grant funded by the Korea government (MIST) (RS-2025-16903034). This work was supported by the National Research Foundation of Korea (NRF) grant funded by the Korea government (MSIT) (RS-2025-23963262). This research was supported by Creative Materials Discovery Program (No. 2017M3D1A1040834) through the National Research Foundation of Korea (NRF) funded by the Ministry of Science and ICT. The Inter-University Semiconductor Research Center, Institute of Engineering Research, and SOFT Foundry Institute at Seoul National University provided research facilities for this work.

Author Contributions Statement

Y.K., Y.J.L., and J.Y. equally contributed this work. J. J. Y., S.L., and H.W.J. supervised this work. B.K. helped phi-scan measurement. S.J.K., J.K., I.I, J.Y.K., H.R., H. K. helped with device characterization. D.S. measured PFM image. C.W.B., M.H.P., and D.H.K. and S.-J.C. revised this manuscript.

Ethics declarations

Competing Interests Statement

The authors declare no competing interests.

ARTICLE IN PRESS

ARTICLE IN PRESS

Figure Legends/Captions (for main text figures)

Figure 1. Comprehensive summary of this study a) Schematic illustration of the CBA structure. **b)** OM image of the CBA sample and SEM image of CBA memristor cells. The scale bars for the device image and OM image are 4 mm and 100 μm, respectively. Two parallel memristor cells are shown, highlighting the target and parasitic current paths. The parasitic current path is blocked by the rectifying current in BBFO. **c)** STEM-HAADF image of the BBFO/SRO interface. The scale bars is 2nm. **d)** Memristive *J*-*V* characteristics measured under a bias range of −5 V to +5 V with the SRO electrode grounded. **e)** Schematic representation of the LTP and LTD behaviors governed by ferroelectric polarization and oxygen vacancies in BBFO. **f)** Cell-to-cell variation in LTP and LTD characteristics evaluated using dot-patterned electrode-devices configured with 39 individual cells. The applied voltage pulses for LTP and LTD measurement were -1.6 V/+1.0 V, with a read voltage of 0.2 V and a pulse duration of 200 μs, **g)** Conductance mapping image displaying the letter B in the selector-free CBA, with the blocked sneak path at S_{13} column illustrated alongside the text image. h) Conductance mapping of individual memristor cells in the 11 x 11 CBA, ranging from 1.98 nS to 10.8 nS, as the number of applied voltage pulses varied from 10 to 100 in increments of 10.

Figure 2. Self-rectifying electrical performance a) Schematic of a unit memristor composed of Pt/BBFO/SRO. The inset shows a STEM-HAADF image of BBFO, with downward arrows indicating the pristine polarization direction. The scale bar is 200pm. **b)** Repetitive *J*-*V* cycling measurements using the BBFO memristor, demonstrating stable operation over 100 cycles. The applied voltage was swept from -5 V to 5 V. **c)** Polarization (*P*) – voltage (*V*) hysteresis curve measured at 100 kHz for the Pt/BBFO/SRO device. **d)** Evolution of band diagrams illustrating the 4 steps of current transport mechanisms corresponding to the *J*-*V* characteristics in Figure 2b. Green circles represent oxygen vacancies, and the arrows in the BBFO band indicate the polarization direction. **e)** Calculated n_t values as a function of temperature based on Table S1 and the following equation, confirming the presence of a donor-like shallow trap state at approximately 0.074 eV. **f)** Energy–density of states diagram constructed based on the band energy analysis.

Figure 3. Artificial synapse performances using BBFO memristor a) Analog DC sweeping measurement showing synaptic potentiation and depression over 15 cycles. The inset presents a magnified view of the positive voltage region to highlight the depression characteristics. **b)** Potentiation/depression characteristics measured by 100 pulse number using BFO and BBFO memristors. The applied programming voltages were -1.6 V/+1.0 V, respectively, with a read voltage of +0.2 V. The pulse duration was 200 μs. The nonlinearity at LTP and LTD (v_{po} and v_{de}) was denoted in Figure 2b, as 0.152 and 0.303, respectively. **c)** SWDP characteristics. The voltage amplitudes of the pulses for synaptic weight potentiation and depression are -1.7 V and +1.1 V, respectively. **d)** Illustration of linearity mechanism in the case of BBFO and BFO memristor. The inset image depicts the oxygen vacancy migration influenced by dipole arrangement in the BBFO.

Figure 4. **Endurable artificial synaptic performance and training results using the BBFO memristor**. **a)** Cycle endurance measurements for LTP/LTD, with 400 pulses applied for each. **b)** Comparison of rectification and state-update endurance between the BBFO device and other memristor-based artificial synaptic devices. **c)** Deep learning simulation results comparing training accuracy for BFO and BBFO synaptic devices. The blue region represents DNN-based training, the yellow region corresponds to CNN-based training, and the purple line indicates numerical training results.

Figure 5. Implementation of the 11×11 BBFO selector-free crossbar array. **a)** Schematic of the selector-free BBFO CBA. **b)** Optical microscope image of the fabricated CBA. The scale bar is 200 μm. **c)** The sneak current blocking mechanism of self-rectifying memristors during CBA operation. Red-colored devices represent reverse-biased elements, blue-colored devices indicate forward-biased elements, and white-colored devices correspond to target cells. **d)** LTP/LTD characteristics of individual CBA cells, with applied pulses of -2.4 V and +1.5 V, respectively. In all cases, the read voltage was +0.2 V, and the pulse duration was 200 μs. **e)** *J*-*V* measurement results for individual cells within the CBA. **f)** Read margin comparison of selector-free CBAs based on BBFO and BFO. The blue line represents BBFO, while the red line corresponds to BFO. **g)** Learning demonstration results using the 11×11 BBFO CBA.

ARTICLE IN PRESS

ARTICLE IN PRESS

Editor's summary:
Neuromorphic computing hardware normally makes an unideal trade-off between energy efficiency, scalability and reliability. Kim et al. report a ferroelectric heterostructure based memristor with near-zero nonlinearity, endurance beyond 10E7 cycles, rectifying ratio exceeding 10E6 and sub-pA off-current.

Peer review information: *Nature Communications* thanks Yishu Zhang (eRef) who co-reviewed with Guobin Zhang (ECR); Cheng Li and the other anonymous reviewer(s) for their contribution to the peer review of this work. A peer review file is available.

ARTICLE IN PRESS